MNRAS **000**, 000–000 (0000) Preprint 5 January 2016 Compiled using MNRAS LaTeX style file v3.0

Galaxy bias from the DES Science Verification Data: combining galaxy density maps and weak lensing maps

C. Chang,[1*†] A. Pujol,[2] E. Gaztañaga,[2] A. Amara,[1] A. Réfrégier,[1]
D. Bacon,[3] M. R. Becker,[4,5] C. Bonnett,[6] J. Carretero,[2,6] F. J. Castander,[2] M. Crocce,[2]
P. Fosalba,[2] T. Giannantonio,[7,8,9] W. Hartley,[1] B. Jain,[10] M. Jarvis,[10] T. Kacprzak,[1]
A. J. Ross,[11] E. Sheldon,[12] M. A. Troxel,[13] V. Vikram,[14] J. Zuntz,[13] T. M. C. Abbott,[15]
F. B. Abdalla,[16,17] S. Allam,[18] J. Annis,[18] A. Benoit-Lévy,[16,19,20] E. Bertin,[19,20]
D. Brooks,[16] E. Buckley-Geer,[18] D. L. Burke,[5,21] D. Capozzi,[3] A. Carnero Rosell,[22,23]
M. Carrasco Kind,[24,25] C. E. Cunha,[5] C. B. D'Andrea,[3,26] L. N. da Costa,[22,23]
S. Desai,[27,28] H. T. Diehl,[18] J. P. Dietrich,[27,28] P. Doel,[16] T. F. Eifler,[10,29] J. Estrada,[18]
A. E. Evrard,[30,31] B. Flaugher,[18] J. Frieman,[18,32] D. A. Goldstein,[33,34] D. Gruen,[5,21,28,35]
R. A. Gruendl,[24,25] G. Gutierrez,[18] K. Honscheid,[11,36] D. J. James,[15] K. Kuehn,[37]
N. Kuropatkin,[18] O. Lahav,[16] T. S. Li,[38] M. Lima,[22,39] J. L. Marshall,[38] P. Martini,[11,36]
P. Melchior,[40] C. J. Miller,[30,31] R. Miquel,[6,41] J. J. Mohr,[27,28,35] R. C. Nichol,[3] B. Nord,[18]
R. Ogando,[22,23] A. A. Plazas,[29] K. Reil,[21] A. K. Romer,[42] A. Roodman,[5,21]
E. S. Rykoff,[5,21] E. Sanchez,[43] V. Scarpine,[18] M. Schubnell,[31] I. Sevilla-Noarbe,[24,43]
R. C. Smith,[15] M. Soares-Santos,[18] F. Sobreira,[18,22] E. Suchyta,[10] M. E. C. Swanson,[25]
G. Tarle,[31] D. Thomas,[3] A. R. Walker[15] (The DES Collaboration)

[*] *e-mail address: chihway.chang@phys.ethz.ch*
[†] *all affiliations at the end of paper*

5 January 2016

ABSTRACT
We measure the redshift evolution of galaxy bias from a magnitude-limited galaxy sample by combining the galaxy density maps and weak lensing shear maps for a $\sim$116 deg^2 area of the Dark Energy Survey (DES) Science Verification data. This method was first developed in Amara et al. (2012) and later re-examined in a companion paper (Pujol et al., in prep) with rigorous simulation tests and analytical treatment of tomographic measurements. In this work we apply this method to the DES SV data and measure the galaxy bias for a magnitude-limited galaxy sample. We find the galaxy bias and 1σ error bars in 4 photometric redshift bins to be 1.33 ± 0.18 ($z=0.2-0.4$), 1.19 ± 0.23 ($z=0.4-0.6$), 0.99 ± 0.36 ($z=0.6-0.8$), and 1.66 ± 0.56 ($z=0.8-1.0$). These measurements are consistent at the 1–2σ level with measurements on the same dataset using galaxy clustering and cross-correlation of galaxies with CMB lensing. In addition, our method provides the only σ_8-independent constraint among the three. We forward-model the main observational effects using mock galaxy catalogs by including shape noise, photo-z errors and masking effects. We show that our bias measurement from the data is consistent with that expected from simulations. With the forthcoming full DES data set, we expect this method to provide additional constraints on the galaxy bias measurement from more traditional methods. Furthermore, in the process of our measurement, we build up a 3D mass map that allows further exploration of the dark matter distribution and its relation to galaxy evolution.

Key words: gravitational lensing: weak – surveys – cosmology: large-scale structure

1 INTRODUCTION

Galaxy bias is one of the key ingredients for describing our observable Universe. In a concordance ΛCDM model, galaxies form at overdensities of the dark matter distribution, suggesting the possibility of simple relations between the distribution of galaxies and dark matter. This particular relation is described by a galaxy bias model (Kaiser 1984). Galaxy bias bridges the observable Universe of galaxies with the underlying dark matter. For a full review of literature on galaxy bias, we refer the readers to Eriksen & Gaztanaga (2015) and references therein.

Observationally, several measurement techniques exist for constraining galaxy bias. The most common approach is to measure galaxy bias through the 2-point correlation function (2PCF) of galaxies (Blake et al. 2008; Simon et al. 2009; Cresswell & Percival 2009; Coupon et al. 2012; Zehavi et al. 2011). Counts-in-cells (CiC) is another method where the higher moments of the galaxy probability density function (PDF) are used to constrain galaxy bias (Blanton 2000; Wild et al. 2005; Swanson et al. 2008). Alternatively, one can combine galaxy clustering with measurements from gravitational lensing, which probes the total (baryonic and dark) matter distribution. Such measurements include combining galaxy clustering with galaxy-galaxy lensing (Simon et al. 2007; Jullo et al. 2012; Mandelbaum et al. 2013) and lensing of the cosmic microwave background (CMB) (Schneider 1998; Giannantonio et al. 2015). The method we present in this work also belongs to this class.

With ongoing and upcoming large galaxy surveys (the Hyper SuprimeCam[1], the Dark Energy Survey[2], the Kilo Degree Survey[3], the Large Synoptic Survey Telescope[4], the Euclid mission[5], the Wide-Field Infrared Survey Telescope[6]), statistical uncertainties on the galaxy bias measurements will decrease significantly. It is thus interesting to explore alternative and independent options of measuring galaxy bias. Such measurements would be powerful tests for systematic uncertainties and break possible degeneracies.

In this paper, we present a new measurement of the redshift-dependent galaxy bias from the Dark Energy Survey (DES) Science Verification (SV) data using a novel method. Our method relies on the cross-correlation between weak lensing shear and galaxy density maps to constrain galaxy bias. The method naturally combines the power of galaxy surveys and weak lensing measurements in a way that only weakly depends on assumptions of the cosmological parameters. In addition, the method involves building up a high-resolution 3D mass map in the survey volume which is interesting for studies of the dark matter distribution at the map level. The relation between the galaxy sample and the mass map also provides information for studies of galaxy evolution.

The analysis in this paper closely follows Amara et al. (2012, hereafter A12) and Pujol et al (in prep, hereafter Paper I). A12 applied this method to COSMOS and zCOSMOS data and discussed different approaches for constructing the galaxy density map and galaxy bias. Paper I carried out a series of simulation tests to explore the regime of the measurement parameters where the method is consistent with 2PCF measurements, while introducing alternative approaches to the methodology. Building on these two papers, this work applies the method to the DES SV data, demonstrating the first constraints with this method using photometric data. Simulations are used side-by-side with data to ensure that each step in the data analysis is robust. In particular, we start with the same set of "ideal" simulations used in Paper I and gradually degrade until they match the data by including noise, photometric redshift errors, and masking effects.

The paper is organized as follows. In §2 we overview the basic principles of our measurement method. In §3 we introduce the data and simulations used in this work. The analysis and results are presented in §4, first with a series of simulation tests and then with the DES SV data. We also present a series of systematics tests here. In §5 we compare our measurements with bias measurements on the same data set using different approaches. We conclude in §6.

2 BACKGROUND THEORY

2.1 Linear galaxy bias

In this work we follow Paper I, where the overdensities of galaxies δ_g is linearly related to the overdensities of dark matter δ at some given smoothing scale R, or

$$\delta_g(z,R) = b(z,R)\delta(z,R). \tag{1}$$

We define $\delta \equiv \frac{\rho-\bar{\rho}}{\bar{\rho}}$, where ρ is the dark matter density and $\bar{\rho}$ is the mean dark matter density at a given redshift. δ_g is defined similarly, with ρ replaced by ρ_g, the number density of galaxies. b can depend on galaxy properties such as luminosity, color and type (Swanson et al. 2008; Cresswell & Percival 2009). This definition is often referred to as the "local bias" model. According to Manera & Gaztañaga (2011), at sufficiently large scales ($\gtrsim$ 40 Mpc/h comoving distance), $b(z,R)$ in Eqn. 1 is consistent with galaxy bias defined through the 2PCF of dark matter (ξ_{dm}) and galaxies (ξ_g). That is, the following equation holds,

$$\xi_g(r) = \langle \delta_g(\boldsymbol{r}_0)\delta_g(\boldsymbol{r}_0+\boldsymbol{r})\rangle = b^2\langle \delta(\boldsymbol{r}_0)\delta(\boldsymbol{r}_0+\boldsymbol{r})\rangle = b^2\xi_{dm}(r), \tag{2}$$

where $\boldsymbol{r}_0$ and $\boldsymbol{r}_0+\boldsymbol{r}$ are two positions on the sky separated by vector $\boldsymbol{r}$. The angle bracket $\langle\rangle$ averages over all pairs of positions on the sky separated by distance $|\boldsymbol{r}| \equiv r$. Our work will be based on scales in this regime.

2.2 Weak Lensing

Weak lensing refers to the coherent distortion, or "shear" of galaxy images caused by large-scale cosmic structures between these galaxies and the observer. Weak lensing probes directly the total mass instead of a proxy of the total mass (e.g. stellar mass, gas mass). For a detailed review of the theoretical background of weak lensing, see e.g. Bartelmann & Schneider (2001).

The main weak lensing observable is the complex shear $\boldsymbol{\gamma} = \gamma_1 + i\gamma_2$, which is estimated by the measured shape of galaxies. The cosmological shear signal is much weaker than the intrinsic galaxy shapes. The uncertainty in the shear estimate due to this intrinsic galaxy shape is referred to as "shape noise", and is often the largest source of uncertainty in lensing measurements. Shear can be converted to convergence, κ, a scalar field that directly measures the projected mass. The convergence at a given position $\boldsymbol{\theta}$ on the sky can be expressed as

$$\kappa(\boldsymbol{\theta},p_s) = \int_0^\infty d\chi\, q(\chi,p_s)\delta(\boldsymbol{\theta},\chi), \tag{3}$$

[1] www.naoj.org/Projects/HSC
[2] www.darkenergysurvey.org
[3] kids.strw.leidenuniv.nl
[4] www.lsst.org
[5] sci.esa.int/euclid
[6] wfirst.gsfc.nasa.gov

where $q(\chi, p_s)$ is the lensing weight

$$q(\chi, p_s) \equiv \frac{3H_0^2\Omega_m\chi}{2c^2a(\chi)} \int_\chi^\infty d\chi_s \frac{\chi_s-\chi}{\chi_s} p_s(\chi_s). \tag{4}$$

Here, χ is the comoving distance, Ω_m is the total matter density of the Universe today normalised by the critical density today, H_0 is the Hubble constant today, and a is the scale factor. $p_s(\chi)$ is the normalized redshift distribution of the "source" galaxy sample where the lensing quantities ($\boldsymbol{\gamma}$ or κ) are measured. In the simple case of a single source redshift plane at χ_s, p_s is a delta function and the lensing weight becomes

$$q(\chi, \chi_s) \equiv \frac{3H_0^2\Omega_m}{2c^2a(\chi)} \frac{\chi(\chi_s-\chi)}{\chi_s}. \tag{5}$$

In the flat-sky approximation, conversion between $\boldsymbol{\gamma}$ and κ in Fourier space follows (Kaiser & Squires 1993, KS conversion):

$$\tilde{\kappa}(\boldsymbol{\ell}) - \tilde{\kappa}_0 = D^*(\boldsymbol{\ell})\tilde{\boldsymbol{\gamma}}(\boldsymbol{\ell}); \;\; \tilde{\boldsymbol{\gamma}}(\boldsymbol{\ell}) - \tilde{\boldsymbol{\gamma}}_0 = D(\boldsymbol{\ell})\tilde{\kappa}(\boldsymbol{\ell}), \tag{6}$$

where "$\tilde{X}$" indicates the Fourier transform of the field X, $\boldsymbol{\ell}$ is the spatial frequency, $\tilde{\kappa}_0$ and $\tilde{\boldsymbol{\gamma}}_0$ are small constant offsets which cannot be reconstructed and are often referred to as the "mass-sheet degeneracy". D is a combination of second moments of $\boldsymbol{\ell}$:

$$D(\boldsymbol{\ell}) = \frac{\ell_1^2 - \ell_2^2 + i2\ell_1\ell_2}{|\boldsymbol{\ell}|^2}. \tag{7}$$

In this work we follow the implementation of Eqn. 6 as described in Vikram et al. (2015) and Chang et al. (2015) to construct κ and $\boldsymbol{\gamma}$ maps as needed.

2.3 κ_g: a convergence template from galaxies

Following the same approach as A12 and Paper I, we now define κ_g by substituting δ with δ_g in Eqn. 3, or

$$\kappa_g(\boldsymbol{\theta}, p_s) = \int_0^\infty d\chi\, q(\chi, p_s)\delta_g(\boldsymbol{\theta}, \chi). \tag{8}$$

Physically, κ_g is a "template" for the convergence κ. In particular, in the case of a constant galaxy bias b, where $\delta_g = b\delta$ everywhere, Eqn. 8 trivially gives $\kappa_g = b\kappa$. The relation between κ, κ_g and b in the case of redshift-dependent galaxy bias (Eqn. 1) becomes more complicated. This requires the introduction of the "partial" κ_g, or κ_g' below. Alternatively, one can adopt the approach used in A12 and include a parametrized galaxy bias model in constructing κ_g.

To construct κ_g', instead of integrating over all foreground "lens" galaxies in Eqn. 8, we only consider the part of the template contributed by a given lens sample. This gives

$$\begin{aligned}\kappa_g'(\boldsymbol{\theta}, \phi', p_s) &= \int_0^\infty d\chi\, q(\chi, p_s)\phi'(\chi)\delta_g(\boldsymbol{\theta}, \chi) \\ &= \int_0^\infty d\chi\, q(\chi, p_s)\phi'(\chi)\left(\frac{\rho_g(\boldsymbol{\theta}, \chi)}{\bar{\rho}_g(\chi)} - 1\right)\end{aligned} \tag{9}$$

where $\phi'(\chi)$ is the radial selection function of the lens sample of interest. ρ_g is the number of galaxies per unit volume and $\bar{\rho}_g$ is the mean of ρ_g at a given redshift. $\phi'(\chi)$ is different from $p'(\chi)$ in Eqn. 20 of Paper I only by a normalization: $\int d\chi p'(\chi) = 1$, while $\phi'(\chi)$ integrates to a length, which is the origin of the $\Delta\chi'$ in Eqn. 20 in Paper I. We choose to use $\phi'(\chi)$ here to facilitate the derivation later, but note that Eqn. 14 below is fully consistent with Eqn. 20 in Paper I. Similarly we define also a partial κ field, which we will later use in §2.4,

$$\kappa'(\boldsymbol{\theta}, \phi', p_s) = \int_0^\infty d\chi\, q(\chi, p_s)\phi'(\chi)\delta(\boldsymbol{\theta}, \chi). \tag{10}$$

In practice, when constructing κ_g', we assume a fixed source redshift $\bar{\chi}_s$ and take the mean lensing weight $\bar{q}'$ and $\bar{\rho}_g$ outside the integration of Eqn. 9. This approximation holds in the case where q and $\bar{\rho}_g$ are slowly varying over the extent of ϕ', which is true for the intermediate redshift ranges we focus on. We have

$$\kappa_g'(\boldsymbol{\theta}, \phi', \bar{\chi}_s) \approx \Delta\chi'\bar{q}'(\bar{\chi}_s)\left(\frac{\int_0^\infty d\chi\phi'(\chi)\rho_g(\boldsymbol{\theta}, \chi)}{\bar{\rho}_g\Delta\chi'} - 1\right), \tag{11}$$

where

$$\Delta\chi' = \int_0^\infty d\chi\phi'(\chi). \tag{12}$$

We further simplify the expression by defining the partial 2D surface density Σ' and $\bar{\Sigma}'$, where

$$\Sigma' = \int_0^\infty d\chi\phi'(\chi)\rho_g(\boldsymbol{\theta}, \chi),\; \bar{\Sigma}' = \int_0^\infty d\chi\phi'(\chi)\bar{\rho}_g. \tag{13}$$

Eqn. 11 then becomes

$$\kappa_g'(\boldsymbol{\theta}, \phi', \bar{\chi}_s) \approx \Delta\chi'\bar{q}'(\bar{\chi}_s)\left(\frac{\Sigma'(\boldsymbol{\theta})}{\bar{\Sigma}'(\boldsymbol{\theta})} - 1\right), \tag{14}$$

which is what we measure as described in §4.1.

2.4 Bias estimation from the galaxy density field and the weak lensing field

The information of galaxy bias can be extracted through the cross- and auto-correlation of the κ and κ_g' fields. (In the case of constant bias, we can replace κ_g' by κ_g in all equations below.) Specifically, we calculate

$$b' = \frac{\langle\kappa_g'\kappa_g'\rangle}{\langle\kappa_g'\kappa\rangle} = \frac{\langle\kappa_g'(\boldsymbol{\theta}, \phi', \bar{\chi}_s)\kappa_g'(\boldsymbol{\theta}, \phi', \bar{\chi}_s)\rangle}{\langle\kappa_g'(\boldsymbol{\theta}, \phi', \bar{\chi}_s)\kappa(\boldsymbol{\theta}, p_s)\rangle}, \tag{15}$$

where $\langle\rangle$ represents a zero-lag correlation between the two fields in the brackets, averaged over a given aperture R. We can write for the most general case,

$$\langle\kappa_A\kappa_B\rangle = \frac{4\pi}{\pi^2R^4}\int_0^R dr_1 r_1 \int_0^R dr_2 r_2 \int_0^\pi d\eta\,\omega_{AB}(\Theta), \tag{16}$$

where κ_A and κ_B can be any of the following: $(\kappa, \kappa', \kappa_g, \kappa_g')$, $\Theta^2 = r_1^2 + r_2^2 - 2r_1r_2\cos\eta$, and $\omega_{AB}(\Theta)$ is the projected two-point angular correlation function between the two fields, defined

$$\omega_{AB}(\Theta) = \int_0^\infty d\chi_A \int_0^\infty d\chi_B q_A q_B \phi_A'\phi_B'\xi_{\kappa_A\kappa_B}(r), \tag{17}$$

where q_A (q_B) and ϕ_A' (ϕ_B') are the lensing weight and lens redshift selection function associated with the fields κ_A (κ_B). $\xi_{\kappa_A\kappa_B}(r)$ is the 3D two-point correlation function. In the case of $\kappa_A = \kappa_B = \kappa$, $\xi_{\kappa_A\kappa_B}$ reduces to ξ_{dm} in Eqn. 2.

For infinitely thin redshift bins, or constant bias, b' in Eqn. 15 directly measures the galaxy bias b of the lens. However, once the lens and source samples span a finite redshift range (see eg. Figure 1), b' is a function of the source and lens distribution and is different from b by some factor $f(\phi', p_s)$, so that

$$b' = f(\phi', p_s)b. \tag{18}$$

Note that f can be determined if $b(z)$ is known. Since we have $b(z) = 1$ for the case of dark matter, we can calculate f by calculating b' and setting $b(z) = 1$, or

$$f(\phi', p_s) = \frac{\langle\kappa'\kappa'\rangle}{\langle\kappa'\kappa\rangle} = \frac{\langle\kappa'(\boldsymbol{\theta}, \phi', \bar{\chi}_s)\kappa'(\boldsymbol{\theta}, \phi', \bar{\chi}_s)\rangle}{\langle\kappa'(\boldsymbol{\theta}, \phi', \bar{\chi}_s)\kappa(\boldsymbol{\theta}, p_s)\rangle}, \tag{19}$$

where κ' is defined in Eqn. 10 and follows the same assumptions in Eqn. 14, where the lensing weight depends on only the mean distance to the source sample $\bar{\chi}_s$. f here corresponds to f_2 in Eqn. 26 in Paper I.

We use a slightly different estimator for b' compared to Eqn. 15 in practice. Combined with Eqn. 18, our estimator for galaxy bias is:

$$b = \frac{1}{f}\frac{\langle \gamma_{\alpha,g}\gamma_{\alpha,g}\rangle - \langle \gamma'^N_{\alpha,g}\gamma'^N_{\alpha,g}\rangle}{\langle \gamma_{\alpha,g}\gamma_{\alpha}\rangle - \langle \gamma'^N_{\alpha,g}\gamma'^N_{\alpha}\rangle}, \qquad (20)$$

where $\alpha = 1,2$ refers to the two components of $\boldsymbol{\gamma}$.

Here we replaced κ' by γ'_α, which is possible since the two quantities are interchangeable through Eqn. 6. The main reason to work with γ'_α is that in our data set, γ'_α is much noisier compared to the κ'_g due to the presence of the shape noise, therefore converting γ'_α to κ'_α would be suboptimal to converting κ'_g to $\gamma'_{\alpha,g}$. This choice depends somewhat on the specific data quality at hand. In addition, the term $\langle \gamma'^N_{\alpha,g}\gamma'^N_{\alpha,g}\rangle$ is introduced to account for the shot noise arising from the finite number of galaxies in the galaxy density field (see also Paper I). The term is calculated by randomizing the galaxy positions when calculating $\gamma'_{\alpha,g}$. Similarly, the $\langle \gamma'^N_{\alpha,g}\gamma'^N_{\alpha}\rangle$ term in the denominator is a small correction that accounts for any spurious correlation that can come from the mask.

The measurement from this method would depend on assumptions of the cosmological model in the construction of κ'_g and the calculation of f. Except for the literal linear dependence on $H_0\Omega_{\rm m}$, due to the ratio nature of the measurement, most other parameters tend to cancel out. Within the current constraints from *Planck*, the uncertainty in the cosmological parameters affect the measurements at the percent level, which is well within the measurement errors ($> 10\%$). All cosmological parameters used in the calculation of this work are consistent with the simulations described in §3.5.

2.5 Multiple source-lens samples

Whereas Eqn. 20 describes how we measure galaxy bias for one source sample and one lens sample, in practice multiple different samples of lenses and the sources are involved. We define several source and lens samples, or "bins", based on their photometric redshift (photo-z), with the lens samples labeled by i and the source samples labeled by j. We use the notation b^α_{ij} to represent the bias measured with γ_α using the source bin j and lens bin i.

Our final estimate of the redshift-dependent galaxy bias and its uncertainty is calculated by combining b^α_{ij} estimates from the two components of shear and all source redshift bins j. We estimate it by taking into account the full covariance between all the measurements of the galaxy bias in the same lens bin i. Our final estimate $\bar{b}_i$ and uncertainty $\sigma(\bar{b}_i)$ quoted are derived via:

$$\bar{b}_i = M_i^T C_i^{-1} D_i [M_i^T C_i^{-1} M_i]^{-1}, \qquad (21)$$

$$\sigma(\bar{b}_i)^2 = (M_i^T C_i^{-1} M_i)^{-1}, \qquad (22)$$

where D is a one dimensional array containing all the measurements $b^i_{\alpha,j}$ of galaxy bias in this lens bin i (including measurement from the two shear components and possibly multiple source bins), M is a 1D array of the same length as D with all elements being 1, and C^{-1} is the unbiased inverse covariant matrix between all $b^i_{\alpha,j}$ measurements, as estimated by Jack-Knife (JK) resampling (Hartlap et al. 2007):

$$D_i = \{b^\alpha_{ij}\}, \;\; \text{all possible } \alpha, j \qquad (23)$$

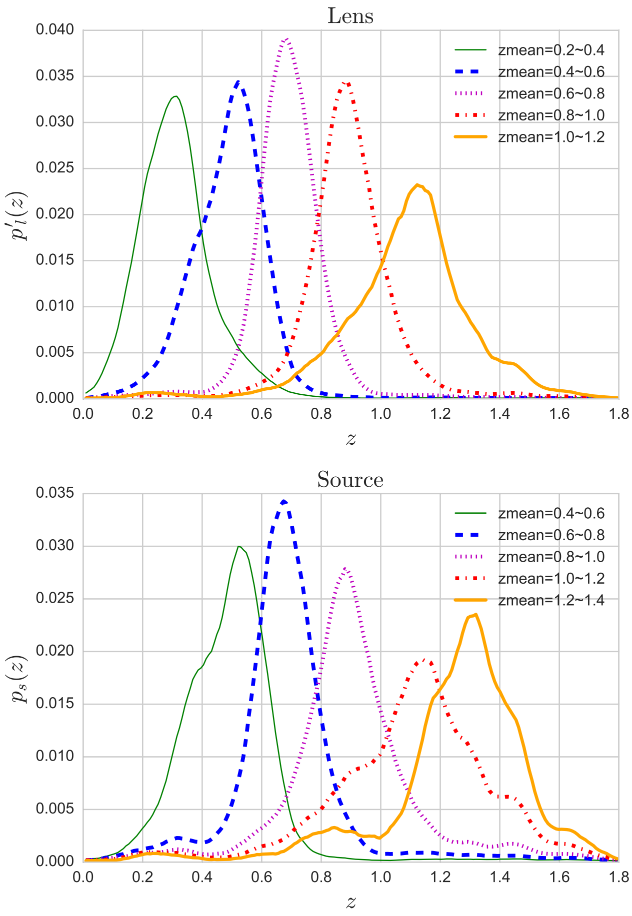

Figure 1. Normalized redshift distribution of the lens (top) and source (bottom) samples as estimated from the photo-z code SKYNET. Each curve represents the stacked PDF for all galaxies in the photo-z bin determined by $z_{\rm mean}$ as listed in the labels.

$$C_i^{-1} = \tau\, {\rm Cov}^{-1}[D_i], \qquad (24)$$

where $\tau = (N - \nu - 2)/(N - 1)$. N is the number of JK samples, and ν is the dimension of C. Note that the matrix inversion of C_i becomes unstable when the measurements b^α_{ij} are highly correlated. This is the case in the noiseless simulations, which we will thus only show the weighted mean of the measurements for our results (Figure 4). For the noisy simulations and data, we quote Eqn. 21 and Eqn. 22 as our results. Also note that in the estimators $\bar{b}_i$ and $\sigma(\bar{b}_i)$ we have not accounted for the correlation between different lens bins i. As we discuss in §4.2, since the main contribution of the covariance comes from the coupling of the mask, noise and large-scale structures in the data, we estimate the covariance from a large number of simulations instead of using the JK method.

3 DATA AND SIMULATIONS

In this section we describe the data and simulation used in this work. We use the DES SV data collected using the Dark Energy Camera (Flaugher et al. 2015) from November 2012 to February 2013 and that have been processed through the Data Management pipeline described in Ngeow et al. (2006); Sevilla et al. (2011); Desai et al. (2012); Mohr et al. (2012). Individual images are stacked, objects are detected and their photometric/morphological properties are measured using the software packages SCAMP (Bertin 2006), SWARP (Bertin et al. 2002), PSFEX (Bertin 2011) and SEXTRACTOR (Bertin & Arnouts 1996). The final product, the SVA1 Gold catalog is the foundation of all catalogs described below. We use a $\sim$116.2 deg^2 subset of the data in the South Pole Telescope East (SPT-E) footprint, which is the largest contiguous region in the SV dataset. This data set is also used in other DES weak lensing and large-scale structure analyzes (Vikram et al. 2015; Chang et al. 2015; Becker et al. 2015; The Dark Energy Survey Collaboration et al. 2015; Crocce et al. 2015; Giannantonio et al. 2015).

3.1 Photo-z catalog

The photo-z of each galaxy is estimated through the SKYNET code (Graff et al. 2014). SKYNET is a machine learning algorithm that has been extensively tested in Sánchez et al. (2014) and Bonnett et al. (2015) to perform well in controlled simulation tests. To test the robustness of our results, we also carry out our main analysis using two other photo-z codes which were tested in Sánchez et al. (2014) and Bonnett et al. (2015): BPZ (Benítez 2000), and TPZ (Carrasco Kind & Brunner 2013, 2014). We discuss in §4.4 the results from these different photo-z codes.

The photo-z codes output a PDF for each galaxy describing the probability of the galaxy being at redshift z. We first use the mean of the PDF, $z_{\rm mean}$ to separate the galaxies into redshift bins, and then use the full PDF to calculate Eqn. 19. In Figure 1, we show the normalized redshift distribution for each lens and source bin as defined below.

3.2 Galaxy catalog

To generate the κ_g maps, we use the same "Benchmark" sample used in Giannantonio et al. (2015) and Crocce et al. (2015). This is a magnitude-limited galaxy sample at $18 < i < 22.5$ derived from the SVA1 Gold catalog with additional cleaning with color, region, and star-galaxy classification cuts (see Crocce et al. 2015, for full details of this sample). The final area is $\sim$ 116.2 square degrees with an average galaxy number density of 5.6 per arcmin^2. Five redshift bins were used from $z_{\rm mean} = 0.2$ to $z_{\rm mean} = 1.2$ with $\Delta z_{\rm mean} = 0.2$. The magnitude-limited sample is constructed by using only the sky regions with limiting magnitude deeper than $i = 22.5$, where the limiting magnitude is estimated by modelling the survey depth as a function of magnitude and magnitude errors (Rykoff et al. 2015). Various systematics tests on the Benchmark has been performed in Crocce et al. (2015) and Leistedt et al. (2015).

3.3 Shear catalog

Two shear catalogs are available for the DES SV data based on two independent shear measurement codes NGMIX (Sheldon 2014) and IM3SHAPE (Zuntz et al. 2013). Both catalogs have been tested rigorously in Jarvis et al. (2015) and have been shown to pass the requirements on the systematic uncertainties for the SV data. Our main analysis is based on NGMIX due to its higher effective number density of galaxies (5.7 per arcmin^2 compared to 3.7 per arcmin^2 for IM3SHAPE). However we check in §4.4.2 that both catalogs produce consistent results. We adopt the selection cuts recommended in Jarvis et al. (2015) for both catalogs. This galaxy sample is therefore consistent with the other DES SV measurements in e.g., Becker et al. (2015); The Dark Energy Survey Collaboration et al. (2015). Similar to these DES SV papers, we perform all our measurements on a blinded catalog (for details of the blinding procedure, see Jarvis et al. (2015)), and only un-blind when the analysis is finalized.

γ_1 and γ_2 maps are generated from the shear catalogs for five redshift bins between $z_{\rm mean} = 0.4$ and $z_{\rm mean} = 1.4$ with $\Delta z_{\rm mean} = 0.2$. Note part of the highest redshift bin lies outside of the recommended photo-z selection according to Bonnett et al. (2015) ($z_{\rm mean} = 0.3 - 1.3$). We discard this bin in the final analysis due to low signal-to-noise (see §4.3), but for future work it would be necessary to validate the entire photo-z range used[7].

3.4 Mask

Two masks are used in this work. First, we apply a common mask to all maps used in this work, we will refer this mask as the *"map mask"*. The mask is constructed by re-pixelating the $i > 22.5$ depth map into the coarser (flat) pixel grid of 5×5 arcmin^2 we use to construct all maps (see §4.1). The depth mask has a much higher resolution (*nside* = 4096 `Healpix` map) than this grid, which means some pixels in the new grid will be partially masked in the original `Healpix` grid. We discard pixels in the new grid with more than half of the area masked in the `Healpix` grid. The remaining partially masked pixels causes effectively a $\sim$ 3% increase in the total area. The partially masked pixels will be taken into account later when generating κ_g (we scale the mean number of galaxy per pixel by the appropriate pixel area). We also discard pixels without any source galaxies.

Pixels on the edges of our mask will be affected by the smoothing we apply to the maps. In addition, when performing the KS conversion, the mask can affect our results. We thus define a second *"bias mask"*, where we start from the *map mask* and further mask pixels that are closer than half a smoothing scale away from any masked pixels except for holes smaller than 1.5 pixels[8]

3.5 Simulations

In this work we use the same mock galaxy catalog from the MICE simulations[9] (Fosalba et al. 2013a; Crocce et al. 2013; Fosalba et al. 2013b) which is described in detail in Paper I. MICE adopts the ΛCDM cosmological parameters: $\Omega_{\rm m} = 0.25$, $\sigma_8 = 0.8$, $n_s = 0.95$, $\Omega_{\rm b} = 0.044$, $\Omega_\Lambda = 0.75$ and $h = 0.7$. The galaxy catalogue has been generated according to a Halo Occupation Distribution (HOD) and a SubHalo Abundance Matching (SHAM) prescription described in Carretero et al. (2015). The main tests were done with the region $0^\circ <$RA$< 30^\circ$, $0^\circ <$Dec$< 30^\circ$, while we use a larger region ($0^\circ <$RA$< 90^\circ$, $0^\circ <$Dec$< 30^\circ$) to estimate the effect from cosmic variance. We use the following properties for each galaxy in

[7] Also note that the lowest redshift lens bin also exceeds the range that is validated. However, since the sample is brighter, the main source of error from depth variation should not be significant.

[8] The reason for not apodizing the small masks is that it would reduce significantly the region unmasked and thus the statistical power of our measurement. We have tested in simulations that the presence of these small holes do not affect our final measurements.. We consider only pixels surviving the *bias mask* when estimating galaxy bias. Figure 2 shows both masks used in this work.

[9] http://cosmohub.pic.es/

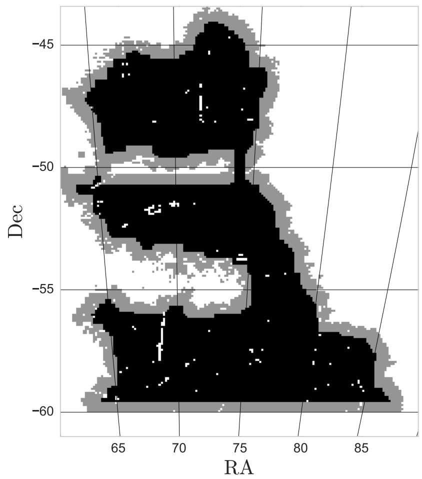

Figure 2. Mask used in this work. The black region shows where the galaxy bias is calculated (the *bias mask*). The black+grey map region is where all maps are made (the *map mask*).

the catalog – position on the sky (RA, Dec), redshift (z), apparent magnitude in the i band, and weak lensing shear ($\boldsymbol{\gamma}$).

In addition, we incorporate shape noise and masking effects that are matched to the data. For shape noise, we draw randomly from the ellipticity distribution in the data and add linearly to the true shear in the mock catalog to yield ellipticity measurements for all galaxies in the mock catalog. We also make sure that the source galaxy number density is matched between simulation and data in each redshift bin. For the mask, we simply apply the same mask from the data to the simulations. Note that the un-masked simulation area is ~ 8 times larger than the data, thus applying the mask increases the statistical uncertainty.

Finally, to investigate the effect of photo-z uncertainties, we add a Gaussian photo-z error to each MICE galaxy according to its true redshift. The standard deviation of the Gaussian uncertainty follows $\sigma(z) = 0.03(1+z)$. This model for the photo-z error is simplistic, but since we use this set of photo-z simulations mainly to test our algorithm (the calculation of f in Eqn. 19), we believe a simple model will serve its purpose.

We note that the larger patch of MICE simulation used in this work ($\sim 30 \times 30$ square degrees) is of the order of what is expected for the first year of DES data ($\sim$2,000 degree square and $\sim$ 1 magnitude shallower). Thus, the simulation measurements shown in this work also serves as a rough forecast for our method applied on the first year of DES data.

4 ANALYSIS AND RESULTS

4.1 Procedure

Before we describe the analysis procedure, it is helpful to have a mental picture of a 3D cube in RA, Dec and z. The z-dimension is illustrated in Figure 1, with a coarse resolution of five redshift bins for both lenses and sources. Each lens and source sample is then collapsed into 2D maps in the RA/Dec-dimension. For each source bin, we can only constrain the galaxy bias using the lens bins at the foreground of this source bin. That is, for the highest source redshift bin there are five corresponding lens bins, and for the lowest source redshift bin there is only one lens bin. The analysis is carried out in the following steps.

First, we generate all the necessary maps for the measurement: γ_1, γ_2 maps for each source redshift bin j, and $\gamma'_{1,g}$, $\gamma'_{2,g}$, $\gamma'^N_{1,g}$, and $\gamma'^N_{2,g}$ maps for each lens bin i and source bin j. We generate random maps ($\gamma'^N_{1,g}$, $\gamma'^N_{2,g}$, γ'^N_1, γ'^N_2) and take the mean of $\langle \gamma'^N_{\alpha,g} \gamma'^N_{\alpha,g} \rangle$ and $\langle \gamma'^N_{\alpha,g} \gamma'^N_{\alpha} \rangle$ in calculating Eqn. 20. All maps are generated using a sinusoidal projection at a reference RA of 71° and 5 arcmin square pixels on the projected plane. These maps are then smoothed by a 50 arcmin boxcar filter while the *map mask* is applied. The chosen pixel and smoothing scales are based on tests described in Paper I. For a given source bin, the value of each pixel in the γ_1 and γ_2 maps is simply the weighted mean of the shear measurements in the area of that pixel. The weights reflect the uncertainties in the shear measurements in the data, while we set all weights to 1 in the simulations. For a given lens bin, the pixel values of the $\gamma'_{1,g}$, $\gamma'_{2,g}$ maps are calculated through Eqn. 14, where Σ' is the number of galaxies in that pixel, and $\bar{\Sigma}'$ is the mean number of galaxies per pixel in that lens bin. For each combination of lens-source bins, we calculate b^{α}_{ij} (Eqn. 20) from the maps after applying the *bias mask*. We assume $\Delta\chi' \approx$ the width of the photo-z bin. f is calculated analytically through Eqn. 19, where we use $\phi'(z) \propto p'_l(z)$, the estimated normalized redshift distribution from our photo-z code for each lens bin.

We combine all estimates for the same lens bin i through Eqn. 21 and Eqn. 22, where the covariance between the different measurements is estimated using 20 JK samples defined with a "k-mean" algorithm (MacQueen 1967). The k-mean method splits a set of numbers (center coordinate of pixels in our case) into several groups of numbers. The split is made so that the numbers in each group is closest to the mean of them. In our analysis it effectively divides our map into areas of nearly equal area, which we use as our JK regions. The different JK samples are slightly correlated due to the smoothing process. We estimate the effect of this smoothing on the error bars by comparing the JK error bars on the zero-lag auto correlation of a random map (with the same size of the data) before and after applying the smoothing. For 20 JK samples, this is a $\sim$10% effect on the error bars, which we will incorporate in the data measurements.

The above procedure is applied to the data and the simulations using the same analysis pipeline.

4.2 Simulation tests

Following the procedure outlined in the previous section, we present here the result of the redshift-dependent galaxy bias measurements from the MICE simulation. We start from an ideal setup in the simulations that is very close to that used in Paper I and gradually degrade the simulations until they match our data. Below we list the series of steps we take:

(i) use the full area (~ 900 deg^2) with the true $\boldsymbol{\gamma}$ maps
(ii) repeat above with photo-z errors included
(iii) repeat above with shape noise included
(iv) repeat above with SV mask applied
(v) repeat above with 12 different SV-like areas on the sky, and vary the shape noise 100 times

Figure 3 illustrates an example of how the $\gamma_{1,g}$ and γ_1 maps degrade over these tests. The left column shows the $\gamma_{1,g}$ maps while the right

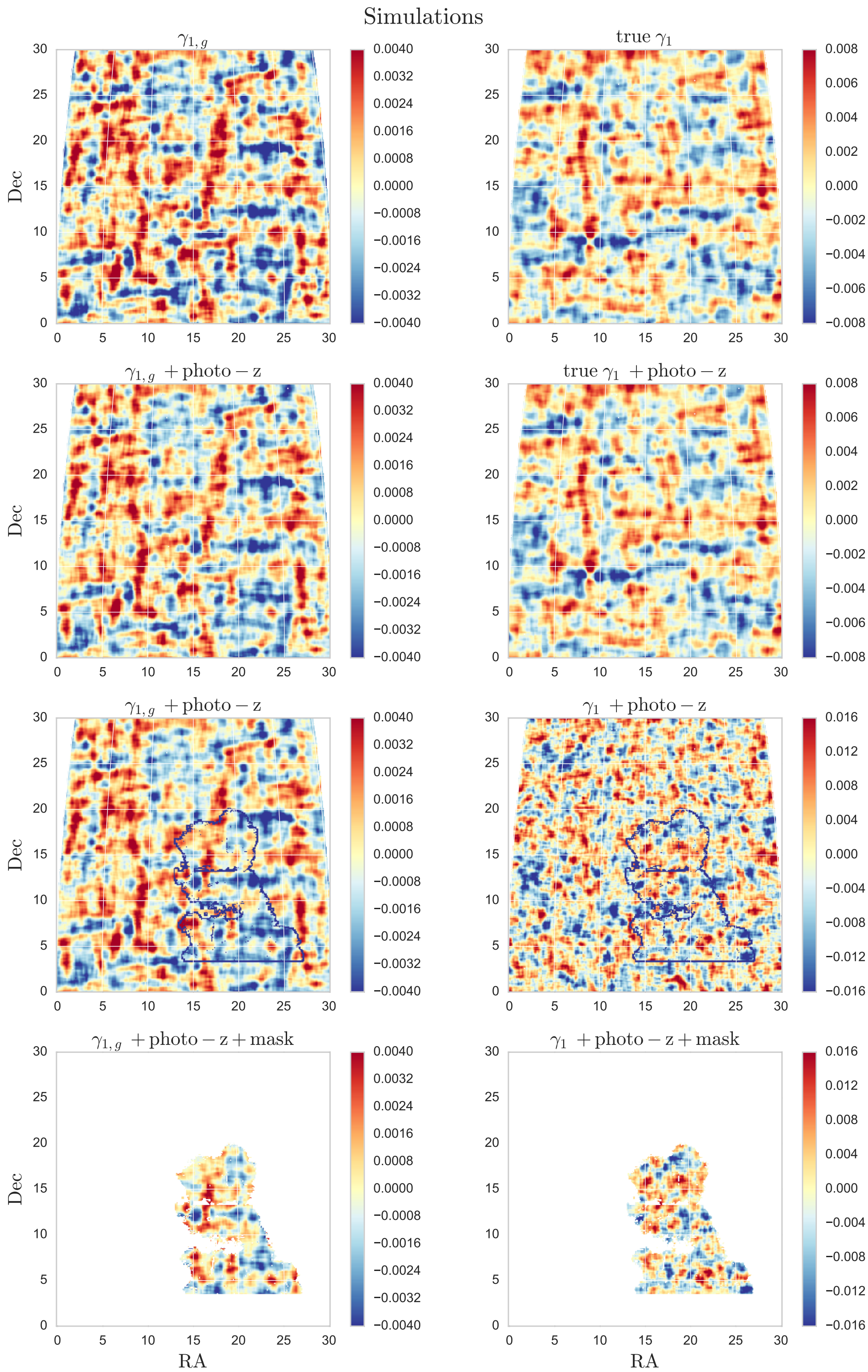

Figure 3. Example of simulation maps used in this work. The left column show $\gamma_{1,g}$ maps and the right column show γ_1 maps. This $\gamma_{1,g}$ maps are generated from the source redshift bin z (or $z_{\rm mean}$)$= 1.0-1.2$ and the lens redshift bin z (or $z_{\rm mean}$)$= 0.4-0.6$. The γ_1 maps are generated from the source redshift bin z (or $z_{\rm mean}$)$= 1.0-1.2$. The galaxy bias for the lens galaxies can be measured by cross-correlating the left and the right column. From top to bottom illustrates the different stages of the degradation of the simulations to match the data. The first row shows the $\gamma_{1,g}$ map against the true γ_1 map for the full 30×30 deg^2 area. The second row shows the same maps with photo-z errors included, slightly smearing out the structures in both maps. The third row shows the same $\gamma_{1,g}$ map as before against the γ_1 that contains shape noise, making the amplitude higher. Finally, the bottom row shows both maps with the SV mask applied, which is also marked in the third row for reference. Note that the color scales on the γ_1 maps is 2 (4) times higher in the upper (lower) two panels than that of the $\gamma_{1,g}$ maps.

column shows the γ_1 maps. Note that the color bars on the upper (lower) two maps in the right panel are 2 (4) times higher compared to the left column. This is to accommodate for the large change in scales on the right arising from shape noise in the γ_1 maps. The first row corresponds to (i) above, and we can visually see the correspondence of some structures between the two maps. Note that the $\gamma_{1,g}$ map only contributes to part of the γ_1 map, which is the reason that we do not expect even the true $\gamma_{1,g}$ and γ_1 maps to agree perfectly. The second row shows the map with photo-z errors included, corresponding to the step (ii). We find that the real structures in the maps are smoothed by the photo-z uncertainties, lowering the amplitude of the map. The smoothing from the photo-z is more visible in the $\gamma_{1,g}$ map, since the γ_1 map probes an integrated effect and is less affected by photo-z errors. The third row shows what happens when shape noise is included, which corresponds to the step (iii) above. We find the structures in the γ_1 map becomes barely visible in the presence of noise, with the amplitude much higher than the noiseless case as expected. The bottom row corresponds to the step (iv) above, where the SV mask is applied to both maps. For the γ_1 map this is merely a decrease in the area. But for the $\gamma_{1,g}$ map, this also affects the conversion from κ_g to $\boldsymbol{\gamma}_g$, causing edge effects in the $\gamma_{1,g}$ map which are visible in the bottom-left map in Figure 3. Step (v) is achieved by moving the mask around and drawing different random realizations of shape noise for the source galaxies.

With all maps generated, we then calculate the redshift-dependent galaxy bias following Eqn. 21 and Eqn. 22 for each of the steps from (i) to (v). In Figure 4 we show the result for the different stages, overlaid with the bias from the 2PCF measurement described in Paper I. In step (i), our measurements recover the 2PCF estimates, confirming the results in Paper I, that we can indeed measure the redshift-dependent bias using this method under appropriate settings. Our error bars are smaller than that in Paper I, which is due to the fact that we have combined measurements from several source bins. Since the only difference between this test and the test in Paper I is the inclusion of the KS conversion, we have also shown that the KS conversion in the noiseless case does not introduce significant problems in our measurements. Although it could be the reason for the slightly lower measurement at redshift bin $0.8-1.0$. The error bars on the highest redshift bin is large due to the small number of source and lens galaxies. In step (ii), we introduce photo-z errors. We find that the photo-z errors do not affect our measurements within the measurement uncertainties. In step (iii), the error bars increase due to the presence of shape noise. In (iv), we apply the SV mask, which causes the error bars to expand and the overall measurement to be lower by slightly more than 1σ. The larger error bars come from the smaller area and the field-to-field variation. The lowered mean value is the result of the noisiness of the denominator of our estimator (Eqn. 20) due to the presence of shape noise and the KS errors from the complicated geometry of the mask. We have additionally checked that without shape noise, the mask alone does not introduce such a strong drop. In (v), we repeat (iv) on 12 different SV-like areas in a larger (30×90 deg^2) simulation area and vary the shape noise 100 times for each. The total 1,200 simulations gives an estimate of the full covariance due to all the measurement effects considered above, and in addition, the coupling between the large-scale structure and the mask geometry. The red points in Figure 4 shows the mean and standard deviation of the 1,200 measurements.

The difference between the 2PCF measurements and (v) (which we refer to as Δb) as well as the error bars of (v) (which we refer to as $\sigma(\Delta b)$) will later be used to calibrate the data measurements in §4.3. We add Δb to the measured values in data, and

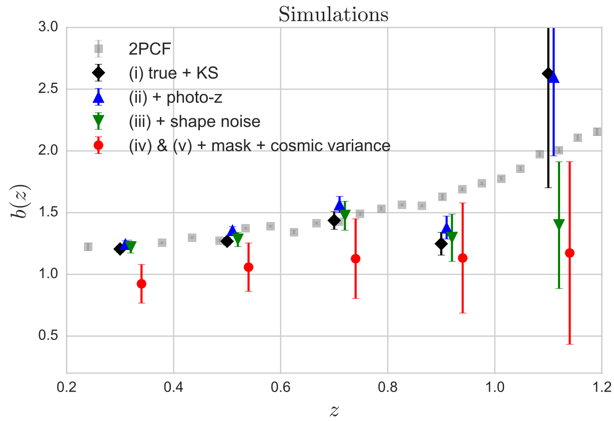

Figure 4. Redshift-dependent galaxy bias measured from simulations with different levels of degradation from the ideal scenario tested in Paper I. The grey line shows the bias from the 2PCF measurement, which we take as "truth". The black, blue, green and red points corresponding to the steps (i), (ii), (iii) and (iv)+(v) in §4.2, respectively. All measurement are done using Eqn. 20.

add in quadrature $\sigma(\Delta b)$ to the uncertainty in our measurements on data. This calibration scheme assumes that we have incorporated the dominant sources of statistical errors in our simulations, which we believe is a valid assumption.

With the series of simulation tests above, we have shown that although the measurement method itself is well grounded, the presence of measurement effects and noise can affect our final results from the data. In the following section we will use what is learned in this section to interpret and correct for the data measurements. Note that all our tests are based on the DES SV data set. With different data characteristics, the interplay between the different effects (photo-z, shape noise, masking, cosmic variance) could be very different.

4.3 Redshift-dependent galaxy bias of DES SV data

We now continue to measure redshift-dependent galaxy bias with the DES SV data using the same procedure as in the simulations. Figure 5 shows some examples of the maps. The right-most panel shows the γ_1 map at redshift bin $z_{\rm mean} = 1.0-1.2$, while the rest of the maps are the $\gamma_{1,g}$ maps at different redshift bin evaluated for this γ_1 map. We see the effect of the lensing kernel clearly: the left-most panel is at the peak of the lensing kernel, giving it a higher weight compared to the other lens bins. We also see correlations between $\gamma_{1,g}$ maps at different redshift bins. This is a result of the photo-z contamination.

In Figure 6 we show the galaxy bias measurement for our magnitude-limited galaxy sample from DES SV together with two other independent measurements with the same galaxy sample (discussed in §5). We have excluded the highest redshift bin since with only a small number of source galaxies, the constraining power from lensing in that bin is very weak. Table 1 summarizes the results. The black data points are from this work, with a best-fit linear model of: $b(z) = 1.35^{\pm0.28} - 0.15^{\pm0.59} z$. As discussed earlier, our method becomes much less constraining going to higher redshift, as the source galaxies become sparse. This is manifested in the increasingly large error bars going to high redshifts. Here we

Table 1. Bias measurement and 1σ error bars from DES SV using the method tested in this work, with all possible lens-source combinations. We also compare here our main measurements with that using alternative shear and photo-z catalogs. Finally we compare our results with other measurement methods carried out on the same data set. The C15 estimates are from Tables 3 in that paper, while the G15 estimates are from Table 2 in that paper.

	Lens redshift ($z_{\rm mean}$)			
	$0.2-0.4$	$0.4-0.6$	$0.6-0.8$	$0.8-1.0$
This work (NGMIX+SKYNET)	$\mathbf{1.33 \pm 0.18}$	$\mathbf{1.19 \pm 0.23}$	$\mathbf{0.99 \pm 0.36}$	$\mathbf{1.66 \pm 0.56}$
This work (IM3SHAPE+SKYNET)	1.37±0.23	1.39±0.29	1.20±0.41	1.47±1.0
This work (NGMIX+TPZ)	1.34±0.18	1.23±0.23	1.00±0.35	1.60±0.55
This work (NGMIX+BPZ)	1.24±0.18	1.16 ±0.23	1.13±0.37	1.41±0.52
Crocce et al. (2015)	1.07 ±0.08	1.24±0.04	1.34±0.05	1.56±0.03
Giannantonio et al. (2015)	0.57 ±0.25	0.91±0.22	0.68±0.28	1.02±0.31

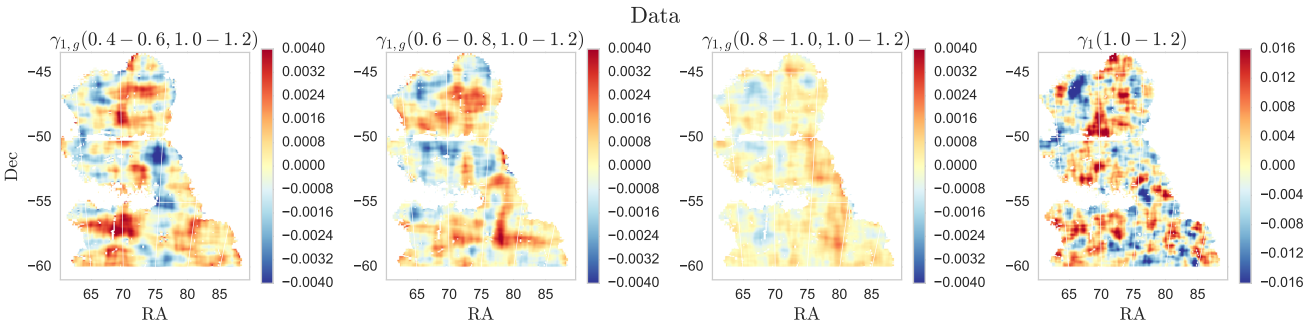

Figure 5. Example of maps from DES SV data. The right-most panel shows the γ_1 map generated from the source redshift bin $z_{\rm mean} = 1.0-1.2$, while the other panels show the $\gamma_{1,g}$ maps generated for the source redshift bin $z_{\rm mean} = 1.0-1.2$ and for different lens redshifts (left: $z_{\rm mean} = 0.4-0.6$, middle: $z_{\rm mean} = 0.6-0.8$, right: $z_{\rm mean} = 0.8-1.0$). The title in each panel for $\gamma_{1,g}$ indicate the lens and source redshift, while the title for γ_1 indicates the source redshift. Note that the color bars are in different ranges, but are matched to the simulation plot in Figure 3. In addition, the left-most and the right-most panels correspond to the bottom row of that figure.

only performed a simple linear fit to the data given the large uncertainties in our measurements. In the future, one could extend to explore more physically motivated galaxy bias models (Matarrese et al. 1997; Clerkin et al. 2015).

In these measurements we include the calibration factor derived from the set of 1,200 SV-like simulations. We find that the spread in the 1,200 simulation measurements is much larger than the error bars on the JK errors on the data measurement itself. This suggests that the field-to-field variation, and how that couples with the mask and the noise is a much larger effect than what the JK errors capture (variation of structure within the field and some level of shape noise). As a result, we have taken the error bars and full covariance from the simulations as our final estimated uncertainty on the measurements.

Compared with A12, our data set is approximately ~105 times larger, but with a (source) galaxy number density ~11.6 times lower. This yields roughly ~ 3 times lower statistical uncertainty in our measurement. Our sample occupies a volume slightly larger than the $0 < z < 1$ sample in A12. Note, however, that due to photo-z uncertainties and the high shape noise per unit area, we expect a slightly higher level of systematic uncertainty in our measurement. Since in A12, the emphasis was not on measuring linear bias, one should take caution in comparing directly our measurement with A12. But we note that the large uncertainties at $z > 0.6$ and the weak constraints on the redshift evolution in the galaxy bias is also seen in A12. To give competitive constraints on the redshift evolution, higher redshift source planes would be needed.

4.4 Other systematics test

In §4.2, we have checked for various forms of systematic effects coming from the KS conversion, finite area, complicated mask geometry, and photo-z errors. Here we perform three additional tests. First, we check that the cross-correlation between the B-mode shear $\boldsymbol{\gamma}_B$ and $\boldsymbol{\gamma}_g$ is small. Next, we check that using the second DES shear pipeline, IM3SHAPE gives consistent answers with that from NGMIX. Finally, we check that using two other photo-z codes also give consistent results. These three tests show that there are no significant systematic errors in our measurements.

4.4.1 B-mode test

Lensing B-mode refers to the divergent-free piece of the lensing field, which is zero in an ideal, noiseless scenario. As a result, B-mode is one of the measures for systematic effects in the data. In Jarvis et al. (2015), a large suite of tests have been carried out to ensure that the shear measurements have lower level of systematic uncertainties compared to the statistical uncertainties. Nevertheless, here we test in specific the B-mode statistics relevant to our measurements.

We construct a $\boldsymbol{\gamma}_B$ field by rotating the shear measurements in our data by 45 degrees, giving:

$$\boldsymbol{\gamma}_B = \gamma_{B,1} + i\gamma_{B,2} = -\gamma_2 + i\gamma_1. \quad (25)$$

Substituting $\boldsymbol{\gamma}_B$ into $\boldsymbol{\gamma}$ in our galaxy bias calculation (Eqn. 20) gives an analogous measurement to b, which we will refer to as b_B. Since we expect $\boldsymbol{\gamma}_B$ not to correlate well with $\boldsymbol{\gamma}_g$, $1/b_B$ would ideally go to zero. In Figure 7, we show all the b_B measurements using both shear component and all lens-source combinations. We see that all the data points as well as the weighted mean are consistent with zero at the 1–2 σ level, assuring that the B-modes in the shear measurements are mostly consistent with noise. We also show the corresponding B-modes from the simulation used in §4.2 (iv), where we see that the level and scatter in the data is compatible with that in the simulations.

4.4.2 IM3SHAPE *test*

As described in §3.3, two independent shear catalogs from DES SV were constructed. Here, we perform the same measurement in our main analysis using the IM3SHAPE catalog. The IM3SHAPE catalog contains less galaxies, thus the measurements are slightly noisier. The resulting redshift-dependent galaxy measurements are shown in Table 1 and are overall slightly higher than the NGMIX measurements, and there is almost no constraining power on the evolution. The best-fit linear bias model is: $b(z) = 1.44^{\pm 0.36} - 0.18^{\pm 0.82} z$, which is very consistent with the NGMIX measurements. The B-modes (not shown here) are similar to Figure 7.

4.4.3 *Photo-z test*

As mentioned in §3.1, several photo-z catalogs were generated for the DES SV data set and shown in Bonnett et al. (2015) to meet the required precision and accuracy for the SV data. All above analyzes were carried out with the SKYNET photo-z catalog. Here we perform the exact same analysis using the other two catalogs: BPZ and TPZ. In specific, to be consistent with the other DES SV analyzes (Becker et al. 2015; The Dark Energy Survey Collaboration et al. 2015), we keep the tomographic bins unchanged (binned by SKYNET mean redshift), but use the $p(z)$ from the different photo-z codes to calculate f. The lensing or galaxy maps themselves remain unchanged.

Table 1 lists the results from the different photo-z catalogs. Since SKYNET and TPZ are both machine learning codes and respond to systematic effects in a similar fashion, while BPZ is a template fitting code, we can thus view the difference between the results from BPZ and the others as a rough measure of the potential systematic uncertainty in our photo-z algorithm (see also discussion in Bonnett et al. 2015), which is shown here to be much smaller than the other sources of uncertainties.

5 COMPARISON WITH OTHER MEASUREMENTS

The redshift-dependent galaxy bias has been measured on the same data set using other approaches. Here we compare our result with two other measurements – galaxy clustering (Crocce et al. 2015, hereafter C15) and cross-correlation of galaxies and CMB lensing (Giannantonio et al. 2015, hereafter G15).We note that both these analyzes assumed the most recent *Planck* cosmological parameters (Planck Collaboration et al. 2014), which is slightly different from our assumptions (see §3.5). But since our measurement depends very weakly on the assumption of cosmological parameters (as discussed in §2.4), the stronger cosmology dependencies come from the cosmological parameters assumed in C15 and G15, which are known well within our measurement uncertainties. We also note that the results we quote in Table 1 are based on the photo-z code TPZ, which means our redshift binning is not completely identical to theirs.

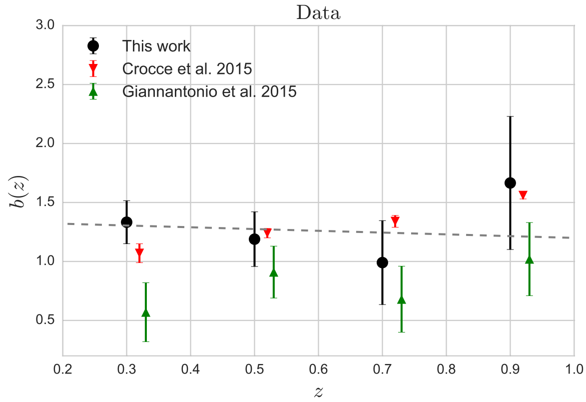

Figure 6. Redshift-dependent bias measured from the DES SV data. The black data points show the result from this work. The red and green points show the measurements on the same galaxy sample with different methods. The grey dashed line is the linear fit to the black data points.

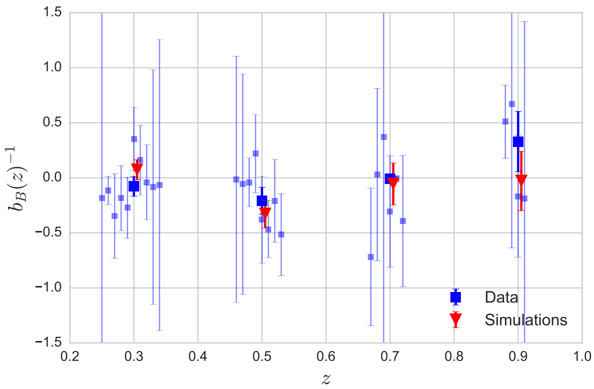

Figure 7. All $1/b_B(z)$ measurements from the B-mode shear and the same γ_g in our main analysis. Each small blue data point represents a measurement from a combination of lens redshift, source redshift, and shear component. Note that the low redshift bins contain more data points, as there are more source galaxies that can be used for the measurement. The large blue points are the weighted mean of all measurements at the same redshift bin from the DES SV data, while the red points are that from simulations that are well matched to data.

5.1 Bias measurement from galaxy clustering

In C15, galaxy bias was estimated through the ratio between the projected galaxy angular correlation function (2PCF) in a given redshift bin and an analytical dark matter angular correlation function predicted at the same redshift. The latter includes both linear and nonlinear dark matter clustering derived from CAMB (Lewis et al. 2000) assuming a set of cosmological parameters. In C15, a flat ΛCDM+ν cosmological model based on *Planck* 2013 + *WMAP* polarization + ACT/SPT + BAO was used. The results in C15 as listed in Table 1 were shown to be consistent with the independent measurement from the CFHTLS (Coupon et al. 2012).

Compared to C15, our work aims to measure directly the local galaxy bias (Eqn. 1) instead of the galaxy bias defined through the 2PCF (Eqn. 2). Although the two measurements agree in the linear regime where this work is based on, comparing the measurements on smaller scales will provide further insight to these galaxy bias models. Our method is less sensitive to assumptions of cosmological parameters compared to the 2PCF method. In particular, it does not depend strongly on σ_8, which breaks the degeneracy between σ_8 and the measured galaxy bias b in other measurement methods. Finally, since our measurement is a cross-correlation method (compared to C15, an auto-correlation method), it suffers less from systematic effects that only contaminate either the lens or the source sample. On the other hand, however, lensing measurements are intrinsically noisy and the conversion between shear and convergence is not well behaved in the presence of noise and complicated masking. In addition, we only considered a one-point estimate (zero-lag correlation), which contains less information compared to the full 2PCF functions. All these effects result in much less constraining power in our measurements.

As shown in Figure 6 and listed in Table 1, our measurements and C15 agree at the 1σ level, with the lowest redshift bin slightly above 1σ. We note, however, both C15 and our work may not have included the complete allocation of systematic errors (especially those coming from the photo-z uncertainties), which could introduce some of the discrepancies.

5.2 Bias measurement from cross-correlation of galaxies and CMB lensing

In G15, galaxy bias is estimated by the ratio between the galaxy-CMB convergence cross-correlation and an analytical prediction of the dark matter-CMB convergence cross-correlation, both calculated through the 2PCF (and also in harmonic space through the power spectrum). Since the lensing efficiency kernel of the CMB is very broad and the CMB lensing maps are typically noisy, this method has less constraining power than C15. However, by using an independent external data, the CMB lensing maps from the South Pole Telescope and the *Planck* satellite, this measurement serves as a good cross check for possible systematic effects in the DES data.

In calculating the theoretical dark matter-CMB convergence cross-correlation, G15 also assumed a fixed cosmology and derived all predictions using CAMB. The σ_8-b degeneracy is thus also present in their analysis. We note, however, that one could apply our method to the CMB lensing data and avoid this dependency. In our framework, the CMB lensing plane will serve as an additional source plane at redshift $\sim$1100. We defer this option to future work.

The results from G15 are shown in Figure 6 and listed in Table 1. These results come from the ratio between the measured and the predicted power spectrum, which suffers less from non-linear effects compared to the measurement in real space (2PCF). We find that G15 is systematically lower than our measurement at the 1σ level for the three highest redshift bin, and shows a much larger discrepancy for the lowest redshift bin. G15 also has more constraining power at high redshift compared to our results, as expected. Possible reasons for the discrepancy at low redshift include systematic errors (in e.g. the photo-z estimation) that are not included in either C15, G15 or this work. In addition, the redshift bins are significantly covariant, making the overall discrepancy less significant. Finally, the scales used in the three studies are slightly different. We refer the readers to G15 for more discussion of this discrepancy.

6 CONCLUSION

In this paper, we present a measurement of redshift-dependent bias using a novel technique of cross-correlating the weak lensing shear maps and the galaxy density maps. The method serves as an alternative measurement to the more conventional techniques such as 2-point galaxy clustering, and is relatively insensitive to the assumed cosmological parameters. The method was first developed in Amara et al. (2012) and later tested more rigorously with simulations in a companion paper (Pujol et al. in prep, Paper I). Here we extend the method and apply it on wide-field photometric galaxy survey data for the first time. We measure the galaxy bias for a magnitude-limited galaxy sample in the Dark Energy Survey (DES) Science Verification (SV) data.

Following from Paper I, we carry out a series of simulation tests which incorporate step-by-step realistic effects in our data including shape noise, photo-z errors and masking. In each step, we investigate the errors introduced in our estimation of galaxy bias. We find that shape noise and masking together affects our measurement in a non-negligible way, causing the galaxy bias to be measured low, while the photo-z affects the measurements in a predictable way if the characteristics of the photo-z uncertainties are well understood. As the measurement itself is very noisy, simulation tests where we know the "truth" provide a good anchor for building the analysis pipeline.

In our main analysis, we measure the galaxy bias with a $18 < i < 22.5$ magnitude-limited galaxy sample in 4 tomographic redshift bins to be 1.33 ± 0.18 ($z = 0.2-0.4$), 1.19 ± 0.23 ($z = 0.4-0.6$), 0.99 ± 0.36 ($z = 0.6-0.8$), and 1.66 ± 0.56 ($z = 0.8-1.0$). Measurements from higher redshifts are too noisy to be constraining. The best-fit linear model gives: $b(z) = 1.36^{\pm 0.31} - 0.08^{\pm 0.70} z$. The results are consistent between different shear and photo-z catalogs.

The galaxy bias of this same galaxy sample has also been measured with two other techniques described in Crocce et al. (2015) and Giannantonio et al. (2015). The three measurements agree at the 1–2σ level at all four redshift bins, though the results from Giannantonio et al. (2015) are systematically lower than our measurements. We note that our method is more constraining at low redshift regions where there are more source galaxies behind the lens galaxies. As pointed out in Amara et al. (2012), to constrain the evolution of galaxy bias, our current data set may not be optimal. A more efficient configuration would be combining a wide, shallow data set with a narrow, deep field. We plan on exploring these possibilities in the future. The main uncertainty in this work comes from the combined effect of masking and shape noise, which we calibrate against simulations with the most important data characteristics incorporated. However, as we demonstrated with simulations, moving to the larger sky coverage of the first and second year of DES data would reduce this effect significantly.

We have demonstrated the feasibility and validity of our method for measuring galaxy bias on a wide-field photometric data set. Looking forward to the first and second year of DES data ($\sim$2,000 square degrees and $\sim$ 1 magnitude shallower), we expect to explore a variety of other topics using this method with the increased statistical power. For example, the same measurement could be carried out on different subsamples of lens galaxies (in magnitude, color, galaxy type etc.) and gain insight into the different clustering properties for different galaxy populations. Also, one can extend the measurement into the non-linear regime and measure the scale-dependencies of the galaxy bias. Finally, it would be interesting to compare the measurement from the 2PCF method and our method (which is a measure of local bias) on different scales to further understand the connections between the two galaxy bias models.

ACKNOWLEDGEMENT

We thank Marc Menera, Donnacha Kirk, Andrina Nicola, Sebastian Seehars for useful discussion and feedback. CC, AA, AR and TK are supported by the Swiss National Science Foundation grants 200021-149442 and 200021-143906. AP was supported by beca FI and 2009-SGR-1398 from Generalitat de Catalunya and project AYA2012-39620 from MICINN. JZ and SB acknowledge support from the European Research Council in the form of a Starting Grant with number 240672.

We are grateful for the extraordinary contributions of our CTIO colleagues and the DECam Construction, Commissioning and Science Verification teams in achieving the excellent instrument and telescope conditions that have made this work possible. The success of this project also relies critically on the expertise and dedication of the DES Data Management group.

Funding for the DES Projects has been provided by the U.S. Department of Energy, the U.S. National Science Foundation, the Ministry of Science and Education of Spain, the Science and Technology Facilities Council of the United Kingdom, the Higher Education Funding Council for England, the National Center for Supercomputing Applications at the University of Illinois at Urbana-Champaign, the Kavli Institute of Cosmological Physics at the University of Chicago, the Center for Cosmology and Astro-Particle Physics at the Ohio State University, the Mitchell Institute for Fundamental Physics and Astronomy at Texas A&M University, Financiadora de Estudos e Projetos, Fundação Carlos Chagas Filho de Amparo à Pesquisa do Estado do Rio de Janeiro, Conselho Nacional de Desenvolvimento Científico e Tecnológico and the Ministério da Ciência, Tecnologia e Inovação, the Deutsche Forschungsgemeinschaft and the Collaborating Institutions in the Dark Energy Survey.

The Collaborating Institutions are Argonne National Laboratory, the University of California at Santa Cruz, the University of Cambridge, Centro de Investigaciones Energéticas, Medioambientales y Tecnológicas-Madrid, the University of Chicago, University College London, the DES-Brazil Consortium, the University of Edinburgh, the Eidgenössische Technische Hochschule (ETH) Zürich, Fermi National Accelerator Laboratory, the University of Illinois at Urbana-Champaign, the Institut de Ciències de l'Espai (IEEC/CSIC), the Institut de Física d'Altes Energies, Lawrence Berkeley National Laboratory, the Ludwig-Maximilians Universität München and the associated Excellence Cluster Universe, the University of Michigan, the National Optical Astronomy Observatory, the University of Nottingham, The Ohio State University, the University of Pennsylvania, the University of Portsmouth, SLAC National Accelerator Laboratory, Stanford University, the University of Sussex, and Texas A&M University.

The DES data management system is supported by the National Science Foundation under Grant Number AST-1138766. The DES participants from Spanish institutions are partially supported by MINECO under grants AYA2012-39559, ESP2013-48274, FPA2013-47986, and Centro de Excelencia Severo Ochoa SEV-2012-0234. Research leading to these results has received funding from the European Research Council under the European Union's Seventh Framework Programme (FP7/2007-2013) including ERC grant agreements 240672, 291329, and 306478.

REFERENCES

Amara A., et al., 2012, MNRAS, 424, 553
Bartelmann M., Schneider P., 2001, Physics Reports, 340, 291
Becker M. R., et al., 2015, preprint, (arXiv:1507.05598)
Benítez N., 2000, ApJ, 536, 571
Bertin E., 2006, in Gabriel C., Arviset C., Ponz D., Enrique S., eds, Astronomical Society of the Pacific Conference Series Vol. 351, Astronomical Data Analysis Software and Systems XV. p. 112
Bertin E., 2011, in Evans I. N., Accomazzi A., Mink D. J., Rots A. H., eds, Astronomical Society of the Pacific Conference Series Vol. 442, Astronomical Data Analysis Software and Systems XX. p. 435
Bertin E., Arnouts S., 1996, A&AS, 117, 393
Bertin E., Mellier Y., Radovich M., Missonnier G., Didelon P., Morin B., 2002, in Bohlender D. A., Durand D., Handley T. H., eds, Astronomical Society of the Pacific Conference Series Vol. 281, Astronomical Data Analysis Software and Systems XI. p. 228
Blake C., Collister A., Lahav O., 2008, MNRAS, 385, 1257
Blanton M., 2000, ApJ, 544, 63
Bonnett C., et al., 2015, preprint, (arXiv:1507.05909)
Carrasco Kind M., Brunner R. J., 2013, MNRAS, 432, 1483
Carrasco Kind M., Brunner R. J., 2014, MNRAS, 442, 3380
Carretero J., Castander F. J., Gaztañaga E., Crocce M., Fosalba P., 2015, MNRAS, 447, 646
Chang C., et al., 2015, Physical Review Letters, 115, 051301
Clerkin L., Kirk D., Lahav O., Abdalla F. B., Gaztañaga E., 2015, MNRAS, 448, 1389
Coupon J., et al., 2012, A&A, 542, A5
Cresswell J. G., Percival W. J., 2009, MNRAS, 392, 682
Crocce M., Castander F. J., Gaztanaga E., Fosalba P., Carretero J., 2013, preprint, (arXiv:1312.2013)
Crocce M., et al., 2015, preprint, (arXiv:1507.05360)
Desai S., et al., 2012, ApJ, 757, 83
Eriksen M., Gaztanaga E., 2015, preprint, (arXiv:1508.00035)
Flaugher B., et al., 2015, AJ, 150, 150
Fosalba P., Crocce M., Gaztanaga E., Castander F. J., 2013a, preprint, (arXiv:1312.1707)
Fosalba P., Gaztanaga E., Castander F. J., Crocce M., 2013b, preprint, (arXiv:1312.2947)
Giannantonio T., et al., 2015, preprint, (arXiv:1507.05551)
Graff P., Feroz F., Hobson M. P., Lasenby A., 2014, MNRAS, 441, 1741
Hartlap J., Simon P., Schneider P., 2007, A&A, 464, 399
Jarvis M., et al., 2015, preprint, (arXiv:1507.05603)
Jullo E., et al., 2012, ApJ, 750, 37
Kaiser N., 1984, ApJ, 284, L9
Kaiser N., Squires G., 1993, ApJ, 404, 441
Leistedt B., et al., 2015, preprint, (arXiv:1507.05647)
Lewis A., Challinor A., Lasenby A., 2000, ApJ, 538, 473
MacQueen J., 1967, in Proceedings of the Fifth Berkeley Symposium on Mathematical Statistics and Probability, Volume 1: Statistics. University of California Press, Berkeley, Calif., pp 281–297, http://projecteuclid.org/euclid.bsmsp/1200512992
Mandelbaum R., Slosar A., Baldauf T., Seljak U., Hirata C. M., Nakajima R., Reyes R., Smith R. E., 2013, MNRAS, 432, 1544
Manera M., Gaztañaga E., 2011, MNRAS, 415, 383
Matarrese S., Coles P., Lucchin F., Moscardini L., 1997, MNRAS, 286, 115
Mohr J. J., et al., 2012. (arXiv:1207.3189), doi:10.1117/12.926785
Ngeow C., et al., 2006. p. 23 (arXiv:astro-ph/0608246), doi:10.1117/12.671017
Planck Collaboration et al., 2014, A&A, 571, A16
Rykoff E. S., Rozo E., Keisler R., 2015, preprint, (arXiv:1509.00870)
Sánchez C., et al., 2014, MNRAS, 445, 1482
Schneider P., 1998, ApJ, 498, 43
Sevilla I., et al., 2011, preprint, (arXiv:1109.6741)
Sheldon E. S., 2014, MNRAS, 444, L25
Simon P., Hetterscheidt M., Schirmer M., Erben T., Schneider P., Wolf C., Meisenheimer K., 2007, A&A, 461, 861
Simon P., Hetterscheidt M., Wolf C., Meisenheimer K., Hildebrandt H.,

Schneider P., Schirmer M., Erben T., 2009, MNRAS, 398, 807
Swanson M. E. C., Tegmark M., Blanton M., Zehavi I., 2008, MNRAS, 385, 1635
The Dark Energy Survey Collaboration et al., 2015, preprint, (arXiv:1507.05552)
Vikram V., et al., 2015, Phys.Rev.D, 92, 022006
Wild V., et al., 2005, MNRAS, 356, 247
Zehavi I., et al., 2011, ApJ, 736, 59
Zuntz J., Kacprzak T., Voigt L., Hirsch M., Rowe B., Bridle S., 2013, MNRAS, 434, 1604

AFFILIATIONS

[1]Department of Physics, ETH Zurich, Wolfgang-Pauli-Strasse 16, CH-8093 Zurich, Switzerland
[2]Institut de Ciències de l'Espai, IEEC-CSIC, Campus UAB, Facultat de Ciències, Torre C5 par-2, 08193 Bellaterra, Barcelona, Spain
[3]Institute of Cosmology & Gravitation, University of Portsmouth, Portsmouth, PO1 3FX, UK
[4]Department of Physics, Stanford University, 382 Via Pueblo Mall, Stanford, CA 94305, USA
[5]Kavli Institute for Particle Astrophysics & Cosmology, P. O. Box 2450, Stanford University, Stanford, CA 94305, USA
[6]Institut de Física d'Altes Energies, Universitat Autònoma de Barcelona, E-08193 Bellaterra, Barcelona, Spain
[7]Institute of Astronomy, University of Cambridge, Madingley Road, Cambridge CB3 0HA, UK
[8]Kavli Institute for Cosmology, University of Cambridge, Madingley Road, Cambridge CB3 0HA, UK
[9]Centre for Theoretical Cosmology, DAMTP, University of Cambridge, Wilberforce Road, Cambridge CB3 0WA, UK
[10]Department of Physics and Astronomy, University of Pennsylvania, Philadelphia, PA 19104, USA
[11]Center for Cosmology and Astro-Particle Physics, The Ohio State University, Columbus, OH 43210, USA
[12]Brookhaven National Laboratory, Bldg 510, Upton, NY 11973, USA
[13]Jodrell Bank Center for Astrophysics, School of Physics and Astronomy, University of Manchester, Oxford Road, Manchester, M13 9PL, UK
[14]Argonne National Laboratory, 9700 South Cass Avenue, Lemont, IL 60439, USA
[15]Cerro Tololo Inter-American Observatory, National Optical Astronomy Observatory, Casilla 603, La Serena, Chile
[16]Department of Physics & Astronomy, University College London, Gower Street, London, WC1E 6BT, UK
[17]Department of Physics and Electronics, Rhodes University, PO Box 94, Grahamstown, 6140, South Africa
[18]Fermi National Accelerator Laboratory, P. O. Box 500, Batavia, IL 60510, USA
[19]CNRS, UMR 7095, Institut d'Astrophysique de Paris, F-75014, Paris, France
[20]Sorbonne Universités, UPMC Univ Paris 06, UMR 7095, Institut d'Astrophysique de Paris, F-75014, Paris, France
[21]SLAC National Accelerator Laboratory, Menlo Park, CA 94025, USA
[22]Laboratório Interinstitucional de e-Astronomia - LIneA, Rua Gal. José Cristino 77, Rio de Janeiro, RJ - 20921-400, Brazil
[23]Observatório Nacional, Rua Gal. José Cristino 77, Rio de Janeiro, RJ - 20921-400, Brazil
[24]Department of Physics, University of Illinois, 1110 W. Green St., Urbana, IL 61801, USA
[25]National Center for Supercomputing Applications, 1205 West Clark St., Urbana, IL 61801, USA
[26]School of Physics and Astronomy, University of Southampton, Southampton, SO17 1BJ, UK
[27]Excellence Cluster Universe, Boltzmannstr. 2, 85748 Garching, Germany
[28]Department of Physics, Ludwig-Maximilians-Universitaet, Scheinerstr. 1, 81679 Muenchen, Germany
[29]Jet Propulsion Laboratory, California Institute of Technology, 4800 Oak Grove Dr., Pasadena, CA 91109, USA
[30]Department of Astronomy, University of Michigan, Ann Arbor, MI 48109, USA
[31]Department of Physics, University of Michigan, Ann Arbor, MI 48109, USA
[32]Kavli Institute for Cosmological Physics, University of Chicago, Chicago, IL 60637, USA
[33]Department of Astronomy, University of California, Berkeley, 501 Campbell Hall, Berkeley, CA 94720, USA
[34]Lawrence Berkeley National Laboratory, 1 Cyclotron Road, Berkeley, CA 94720, USA
[35]Max Planck Institute for Extraterrestrial Physics, Giessenbachstrasse, 85748 Garching, Germany
[36]Department of Physics, The Ohio State University, Columbus, OH 43210, USA
[37]Australian Astronomical Observatory, North Ryde, NSW 2113, Australia
[38]George P. and Cynthia Woods Mitchell Institute for Fundamental Physics and Astronomy, and Department of Physics and Astronomy, Texas A&M University, College Station, TX 77843, USA
[39]Departamento de Física Matemática, Instituto de Física, Universidade de São Paulo, CP 66318, CEP 05314-970, São Paulo, SP, Brazil
[40]Department of Astrophysical Sciences, Princeton University, Peyton Hall, Princeton, NJ 08544, USA
[41]Institució Catalana de Recerca i Estudis Avançats, E-08010 Barcelona, Spain
[42]Department of Physics and Astronomy, Pevensey Building, University of Sussex, Brighton, BN1 9QH, UK
[43]Centro de Investigaciones Energéticas, Medioambientales y Tecnológicas (CIEMAT), Madrid, Spain